



# Global impact of benthic denitrification on marine $N_2$ fixation and primary production simulated by a variable-stoichiometry Earth system model

Na Li<sup>1</sup>, Christopher J. Somes<sup>1</sup>, Angela Landolfi<sup>2</sup>, Chia-Te Chien<sup>1</sup>, Markus Pahlow<sup>1</sup>, and Andreas Oschlies<sup>1</sup>

<sup>1</sup>GEOMAR Helmholtz Centre for Ocean Research Kiel, Kiel, Germany

<sup>2</sup>Institute of Marine Sciences (ISMAR), CNR, Rome, Italy

**Correspondence:** Na Li (nli@geomar.de)

**Abstract.** Nitrogen (N) is a crucial limiting nutrient for phytoplankton growth in the ocean. The main source of bioavailable N in the ocean is delivered by  $N_2$ -fixing diazotrophs in the surface layer. Since field observation of  $N_2$  fixation are spatially and temporally sparse, the fundamental processes and mechanisms controlling  $N_2$  fixation are not well understood and constrained. Here, we implement benthic denitrification in an Earth System Model of intermediate complexity (UVic-ESCM 2.9) coupled to an optimality-based plankton ecosystem model (OPEM v1.1). Benthic denitrification occurs mostly in coastal upwelling regions and on shallow continental shelves, and is the largest N-loss process in the global ocean. We calibrate our model against three different combinations of observed Chl,  $NO_3^-$ ,  $PO_4^{3-}$ ,  $O_2$  and  $N^* = NO_3^- - 16PO_4^{3-} + 2.9$ . The inclusion of  $N^*$  provides a powerful constraint on biogeochemical model behavior. Our new model version including benthic denitrification simulates higher global rates of  $N_2$  fixation with a more realistic distribution extending to higher latitudes that are supported by independent estimates based on geochemical data. Oxygen deficient zone volume and water column denitrification rates are reduced in the new version, indicating that including benthic denitrification may improve global biogeochemical models that commonly overestimate anoxic zones. With the improved representation of the ocean N cycle, our new model configuration also yields better global net primary production (NPP) when compared to the independent datasets not included in the calibration. Benthic denitrification plays an important role shaping  $N_2$  fixation and NPP throughout the global ocean in our model, and should be considered when evaluating and predicting their response to environmental change.

## 1 Introduction

Nitrogen is a major limiting nutrient for phytoplankton growth throughout the majority of the tropical and subtropical oceans.  $N_2$  fixation by photo-autotrophic cyanobacteria supplies the ocean with most of its bio-available N (Fig. 1). The main loss processes of fixed N are denitrification and anammox, which occur under low-oxygen conditions in the water column and sediment pore-waters. In recent decades, numerous studies have been conducted to investigate water-column denitrification and anammox inside oxygen deficient zones (ODZs). These studies have explored various aspects, including genomes, metabolism pathways and their rates, and microbial community structure, utilizing a range of modeling approaches (Hutchins and Capone,



2022). Research on benthic denitrification has been more limited, however, even though the greater part of global ocean denitrification ( $\approx 60 - 75\%$ ) occurs in the sediments (Somes et al., 2013; DeVries et al., 2013; Eugster and Gruber, 2012; Brandes and Devol, 2002). Benthic denitrification is involved in N-cycle stabilizing feedbacks over centennial timescales (Landolfi et al., 2017), and occurs primarily on continental shelves (Middelburg et al., 1996), where a high flux of particulate organic matter fuels the depletion of oxygen in sediment pore-waters. Hence, this process is particularly susceptible to the impacts of human activities. Nevertheless, benthic denitrification is often not evaluated in the analysis of  $N_2$  fixation (e.g., Bopp et al., 2022; Hamilton et al., 2020; Paulsen et al., 2017) or not included in current global biogeochemical models (e.g., Pahlow et al., 2020; Hajima et al., 2020; Dutkiewicz et al., 2015; Landolfi et al., 2013).

In the marine nitrogen cycle, N-loss processes convert bioavailable N to dinitrogen gas that creates a N deficiency compared to phosphate. With their activity  $N_2$  fixers replenish the nitrogen deficit in the surface ocean (Somes et al., 2013). Reproducing realistic patterns and rates of denitrification will be an important aspect for simulating  $N_2$  fixation. In the ocean, a measure of the N deficit is generally expressed by the geochemical tracer  $N^*$  (Gruber and Sarmiento, 1997), the deviation of nitrate relative to phosphate with respect to the Redfield N:P ratio (Redfield, 1934). Therefore, the distribution of  $N^*$  has been used to infer rates of  $N_2$  fixation and denitrification (e.g., Gruber and Sarmiento, 1997; Deutsch et al., 2007; Landolfi et al., 2008; Wang et al., 2019). Contrasting these geochemical inversion estimations, we aim to test the ability of  $N^*$  to constrain our prognostic model that includes the representation of large-scale stoichiometric diversity of phytoplankton and diazotrophs (Pahlow et al., 2020).

Projections of how  $N_2$  fixation evolves under global warming in current Earth system models are highly uncertain (Wrightson and Tagliabue, 2020). Since  $N_2$  fixation can supply the N-limited surface waters with bioavailable nitrogen, it can have a strong impact on how NPP responds to climate change (Bopp et al., 2022; Landolfi et al., 2017). This suggests that a robust understanding of  $N_2$  fixation and how it may respond to climate change is essential to predicting future changes in ocean NPP. The global impact of benthic denitrification on  $N_2$  fixation and NPP is thus a major focus of this paper.

In this study, we have implemented an empirical parameterization for benthic denitrification (Bohlen et al., 2012) into a global ocean biogeochemical model with an explicit phytoplankton and diazotroph physiology (OPEM, (Pahlow et al., 2020)). We calibrate the model by conducting a large ensemble of simulations, whose parameter sets have been constructed via Latin-hypercube sampling, and select the three best simulations according to an objective cost function based on different combinations of global observational datasets including  $N^*$ . These simulations significantly improve not only the global N cycle, but also other important aspects of global marine biogeochemistry compared to the original OPEM without benthic denitrification. We explore model uncertainty by contrasting the behaviour of our three optimized solutions. Finally, we discuss limitations and possible future developments.



## 2 Model description

We use the optimality-based plankton ecosystem model (OPEM, Pahlow et al., 2020) which is incorporated into the UVic  
55 model version 2.9 (Weaver et al., 2001; Eby et al., 2009, 2013). Below we provide a brief description the original OPEM  
implementation in UVic 2.9 (Pahlow et al., 2020), followed by the newly-implemented benthic denitrification.

### 2.1 Physical configuration

The physical circulation configuration remains identical to previous UVic 2.9 Kiel versions (Pahlow et al., 2020; Nickelsen  
et al., 2015). The model has a horizontal resolution of  $1.8^\circ$  latitude  $\times$   $3.6^\circ$  longitude, and the ocean component has nineteen  
60 levels in the vertical with thicknesses ranging from 50m near the surface to 500m in the deep ocean. The physical circulation  
model contains the zonally anisotropic isopycnal viscosity and diffusivity schemes to better reproduce equatorial undercur-  
rents (Getzlaff and Dietze, 2013; Somes et al., 2010b). The atmospheric component consists of a simple 2D energy-moisture  
balance scheme with prescribed wind fields. The physical ocean model is forced by an observation-based monthly wind stress  
reconstruction (Kalnay et al., 1996). Atmospheric  $p\text{CO}_2$  is prescribed and kept fixed at 284 ppm.

### 65 2.2 Optimality-based Plankton Ecosystem Model

The OPEM contains an optimality-based model (Pahlow et al., 2013) for non- $\text{N}_2$ -fixing phytoplankton and diazotrophs with  
variable stoichiometry and an optimal current-feeding model (Pahlow and Prowe, 2010) with homeostatic stoichiometry and  
variable assimilation efficiency for the only zooplankton group. Phytoplankton and facultative diazotrophs allocate their re-  
sources optimally to maximize their net growth rates under different ambient environmental conditions. In contrast to the  
70 fixed-stoichiometry plankton-ecosystem implementation in UVic 2.9 (Keller et al., 2012), OPEM does not impose a priori a  
lower potential growth rate on diazotrophs than non- $\text{N}_2$ -fixing phytoplankton, although the high cost of  $\text{N}_2$  fixation (Pahlow  
et al., 2013) has a similar effect. OPEM also accounts for variable stoichiometry of detritus and the associated remineraliza-  
tion.  $\text{O}_2$  consumption for particulate organic matter decomposition is linked to contributions of C and N remineralization with  
respiratory quotients of  $r_{-\text{O}_2:\text{C}} = 1.15$  and  $r_{-\text{O}_2:\text{N}} = 2$ , respectively.

75 The temperature dependence is from the OPEM-H configuration of Pahlow et al. (2020), where growth and nutrient uptake  
of phytoplankton and diazotrophs follow the same exponential Eppley (1972) temperature function but  $\text{N}_2$  fixation is driven  
by the unimodal function of Houlton et al. (2008) with an optimal temperature of  $26^\circ\text{C}$ . Half-saturation iron concentrations of  
phytoplankton and diazotrophs are global constants and calibrated as described in Section 2.4.

### 2.3 Benthic denitrification implementation

80 We include benthic denitrification as a transfer function, which has been empirically derived from benthic flux measurements  
(Bohlen et al., 2012). Denitrification scales linearly with the rain rate of particulate organic carbon deposited on the seafloor  
(RRPOC) and is amplified in environments with low oxygen and high nitrate levels. We apply the transfer function with the  
parameters obtained by Bohlen et al. (2012), same as those implemented in (Somes and Oschlies, 2015) but differ slightly from



the preliminary implementation in Somes et al. (2013). Anammox is implicitly accounted for in the denitrification estimate  
85 since this parameterization is designed to capture total fixed-N loss (Bohlen et al., 2012; Koeve and Kähler, 2010) and our  
model does not differentiate between different species of dissolved inorganic nitrogen. We apply a sub-grid scale bathymetry  
scheme where the effect of the unresolved high-resolution bathymetry is parameterized by multiplying with the area-fraction  
of the sea-floor in each grid cell (Somes et al., 2013; Somes and Oschlies, 2015). This is crucial for resolving high benthic  
denitrification rates over continental shelves smaller than the coarse-resolution model bathymetry.

## 90 2.4 Model calibration

### 2.4.1 Ensemble simulation setup

Our parameter settings are based on the OPEM-H configuration of (Pahlow et al., 2020; Chien et al., 2020). In order to allow  
for a wider range of physiological differences between phytoplankton and diazotrophs, we increase the number of parameters  
to be calibrated by 5 from the pilot work. Thus, we vary 18 parameters in total (Table 1).

95 The additional parameters are potential light affinity of phytoplankton ( $\alpha_{\text{phy}}$ ) and diazotrophs ( $\alpha_{\text{dia}}$ ), diazotroph half-saturation  
constant for Fe ( $k_{\text{Fe,dia}}$ ), diazotroph potential nutrient affinity ( $A_{0,\text{dia}}$ ), and linear increase of sinking speed with depth ( $w_{\text{dd}}$ ).  
We allow diazotroph and phytoplankton parameters to vary independently, using the same ranges for phytoplankton and dia-  
zotrophs and only impose the restriction  $1 \leq k_{\text{Fe,dia}}/k_{\text{Fe,phy}} \leq 3$ . This allows further decoupling of phytoplankton and diazotroph  
physiology compared to Chien et al. (2020) and Pahlow et al. (2020), who assumed that  $k_{\text{Fe,dia}}$  and  $A_{0,\text{dia}}$  co-vary with their  
100 phytoplankton equivalents. Additionally, we allow a 50% overlap between the ranges of zooplankton grazing preference for  
diazotrophs and phytoplankton (Table 1) to enable a certain degree of freedom for these highly-uncertain parameters.

The subsistence nutrient quotas ( $Q_{0,\text{phy}}^{\text{N}}$ ,  $Q_{0,\text{phy}}^{\text{P}}$ ,  $Q_{0,\text{dia}}^{\text{N}}$ , and  $Q_{0,\text{dia}}^{\text{P}}$ ) are the minimum quotas for maintaining cellular integrity.  
The subsistence P quota range is the same for diazotrophs and phytoplankton, while the diazotrophs' subsistence N quota range  
is much higher than that of phytoplankton, and also than the range used by Pahlow et al. (2020). This setting is more consistent  
105 with the earlier estimates (Pahlow et al., 2013) obtained by calibration with lab-culture data for *Trichodesmium* (Holl and  
Montoya, 2008; Mulholland and Bernhardt, 2005).

We use the ranges of these parameters to generate a Latin-hypercube ensemble of 600 different combinations of the 18  
parameters selected for calibration. While the Latin-hypercube method is efficient for evenly sampling a large-dimensional  
space, our 600 parameter sets provide only a very sparse coverage of this 18-dimensional parameter space, but we use this as  
110 a pragmatic choice to obtain information about suitable parameter regions.

Every ensemble member has been spun-up with pre-industrial (AD 1850) boundary conditions with fixed atmospheric  $\text{pCO}_2$   
of 284 ppm for 10,000 years. After the spin-up, we integrate for another year and use annual and monthly means of year 10,001  
for model evaluation and analysis. Due to the simple atmospheric model that is driven by prescribed winds, the model has  
virtually no internal interannual variability, making this short analysis period a pragmatic choice.





## 115 2.4.2 Cost functions

To assess the model performance with respect to the spatial distributions of dissolved tracers and surface chlorophyll *a*, we apply global misfit metrics *J* based on a maximum-likelihood estimation (ML) method for parameters, assuming log-normally distributed errors, with observations grouped by distinct biogeochemical biomes (Fay and McKinley, 2014) as described in Chien et al. (2020). Briefly, the calculation of our cost function comprises two terms for every depth level in our model,

$$120 \quad J_k = \mathbf{d}_k^T \mathbf{R}_k^{-1} \mathbf{d}_k + \mathbf{v}_k^T \mathbf{V}_k^{-1} \mathbf{v}_k, \quad k \in \{1, 2, \dots, 19\} \quad (1)$$

where the residual (*d*) between observations (*o*) and the model (*m*) within each biome is defined as  $\mathbf{d} = \mathbf{o} - \mathbf{m}$ , and the discrepancy in the spatial variance (*v*) as  $\mathbf{v} = v(\mathbf{o}) - v(\mathbf{m})$ . For each variable included in the cost function, we normalize the concentrations to threshold values and log-transform to achieve approximately Gaussian error distributions for *d* and *v* with zero mean and covariance matrices **R** and **V**, respectively. We integrate the results across the 17 biomes, applying Eq. (1) to  
125 monthly means for the upper 550m (top 5 layers in UVic) and annual means below (bottom 14 layers).

We apply the cost function to calibrate model solutions against three different combinations of types of observations. The first is identical to that employed by Chien et al. (2020), who chose four types of observations, i.e., nitrate, phosphate, and oxygen measurements from the World Ocean Atlas 2013 (Garcia et al., 2013a, b) and remote sensing-derived surface chlorophyll concentration (NASA Goddard Space Flight Center et al., 2014). For the second, we use only  $N^* = NO_3^- - 16 \cdot PO_4^{3-} + 2.9$   
130 (Gruber and Sarmiento, 1997), which relates to several processes including  $N_2$  fixation and denitrification (e.g., Landolfi et al., 2008), to test the efficacy of  $N^*$  for assessing model solutions. The third is the same as the first, except that we replace nitrate with  $N^*$ . With these three calibrated solutions, we are able to characterize model uncertainty with respect to which observations are used for calibration.

## 3 Results and discussion

### 135 3.1 Ranges of global tracers and fluxes of the ensemble simulations

Within the 600 ensemble simulations, many tracer concentrations and fluxes, span wide ranges (Fig. 2) except phosphate because phosphorus is conserved in the model. Globally averaged  $NO_3^-$  varies by a factor of 5 and  $N^*$  varies from -23 to 12.5  $mmol\ m^{-3}$  for the different parameter combinations.  $O_2$  varies by a factor of 2, NPP by a factor of 4, globally integrated  $N_2$  fixation rates by a factor of 10, benthic denitrification by a factor of 4, and water-column denitrification from 0 to 276  
140  $Tg\ N\ yr^{-1}$ . The differences between  $N_2$  fixation and denitrification among all simulations range from -11.8 to 5  $Tg\ N\ yr^{-1}$ , which indicates a slight imbalance at the end of the spin-up. The net fixed-N fluxes relative to  $N_2$  fixation rates (N imbalance /  $N_2$  fixation) range from -10% to 4% with a median of 0.3%, in line with our steady-state assumption.

The different cost metrics yield similar optimal solutions (lowest cost function) for globally averaged  $NO_3^-$ ,  $PO_4^{3-}$ ,  $N^*$  and  $O_2$  (Fig. 2 and Table 1). The sharp gradients around the optimal solutions of global  $NO_3^-$  and  $N^*$  illustrate the strong constraints  
145 the cost function provides for these two tracers. In contrast to the original OPEM-H configuration (Fig. 4 in Chien et al.,



2020), the majority of the globally averaged  $\text{NO}_3^-$  simulations underestimate the observational average. Thus, our new model configuration with benthic denitrification has a stronger tendency to lose fixed N relative to original OPEM-H configuration without benthic denitrification, which one might expect from the incorporation of the additional N loss process.

### 3.2 Best models choices

150 We identify three optimal model solutions  $\text{calib\_NO}_3^-$ ,  $\text{calib\_N}^*$ \_only,  $\text{calib\_N}^*$ , based on the three cost functions that include different sets of observations, and compare these with the OPEM-H configuration without benthic denitrification ( $\text{no\_bdeni}$ ) (Table 2 and Fig. 2) and observations (Fig. 2).

Our solutions  $\text{calib\_N}^*$ \_only and  $\text{calib\_N}^*$  appear better constrained than  $\text{calib\_NO}_3^-$  (Fig. 2a, b and c). Globally-averaged nitrate concentrations of  $\text{calib\_N}^*$ \_only and  $\text{calib\_N}^*$  are closer to the WOA13 average of  $31.0 \text{ mmol m}^{-3}$  than  $\text{calib\_NO}_3^-$ ,  
155 although  $\text{calib\_NO}_3^-$  is calibrated directly against observed nitrate, whereas  $\text{calib\_N}^*$ \_only and  $\text{calib\_N}^*$  consider nitrate only indirectly via  $\text{N}^*$ . Globally-averaged oxygen concentrations range from  $183.5$  to  $195.7 \text{ mmol m}^{-3}$ , slightly above the observed WOA13 value of  $176 \text{ mmol m}^{-3}$ . Interestingly,  $\text{O}_2$  is also quite well constrained in  $\text{calib\_N}^*$ \_only (Fig. 2c and Table 2), although it is calibrated only against  $\text{N}^*$ .

While the inventory of nitrogen is essentially identical among the three optimal model solutions, the nitrogen fluxes vary  
160 widely. The calibrated estimates for water-column denitrification are more variable ( $2.8$ – $69.5 \text{ Tg N yr}^{-1}$ ) than for benthic denitrification ( $91.4$ – $105.5 \text{ Tg N yr}^{-1}$ ). This relatively weak constraint on water-column denitrification was also reported by Chien et al. (2020), who used an additional objective to constrain water-column denitrification to values above  $60 \text{ Tg N yr}^{-1}$  ( $\text{no\_bdeni}$  in Table 2). Correspondingly, the addition of benthic denitrification allows much higher estimates of global  $\text{N}_2$  fixation than  $\text{no\_bdeni}$ .

165 The high variability of water-column denitrification is much reduced in  $\text{calib\_N}^*$ \_only and  $\text{calib\_N}^*$ , ranging from  $30.3$  to  $42.4 \text{ Tg N yr}^{-1}$ , hence varying similarly to our benthic denitrification estimates of  $94.4$ – $105.5 \text{ Tg N yr}^{-1}$ . Thus, incorporating  $\text{N}^*$  into the calibration objective helps reduce the uncertainty of ocean nitrogen fluxes, particularly water-column denitrification. Moreover, using  $\text{N}^*$  also yields more reasonable rates of water-column denitrification and global  $\text{N}_2$  fixation. Globally integrated water-column denitrification has been estimated between  $39$ – $77 \text{ Tg N yr}^{-1}$  (Eugster and Gruber, 2012;  
170 DeVries et al., 2012, 2013; Somes et al., 2013; Wang et al., 2019). This suggests that  $\text{N}^*$  provides a more powerful constraint on water-column denitrification rates, and hence  $\text{N}_2$  fixation, than simply combining  $\text{NO}_3^-$  and  $\text{PO}_4^{3-}$ .

With the representation of benthic denitrification in our model and the inclusion of  $\text{N}^*$  into our cost function, global  $\text{N}_2$  fixation rates are between  $136.1$ – $137.7 \text{ Tg N yr}^{-1}$ , which is close to previous estimates of  $137 \text{ Tg N yr}^{-1}$  (Deutsch et al., 2007) and  $163 \text{ Tg N yr}^{-1}$  (Wang et al., 2019). Our estimates also fall within the range of extrapolations of direct measurements,  
175 which yield marine  $\text{N}_2$  fixation rates between  $131$  and  $253 \text{ Tg N yr}^{-1}$  (Großkopf et al., 2012; Luo et al., 2012; Shao et al., 2023).

Globally-integrated net primary production (NPP) rates among our three calibrated simulations are consistently lower than that of  $\text{no\_bdeni}$  ( $88 \text{ Pg C yr}^{-1}$ ), from  $52.8$  to  $63.0 \text{ Pg C yr}^{-1}$ . This is much closer to observation-based estimates of  $52$  (satellite-based, Silsbe et al., 2016) and  $53 \text{ Pg C yr}^{-1}$  (derived from Argo oxygen measurements, Johnson and Bif, 2021). The



180 new estimates of export production at 130m (model euphotic depth) are relatively close to and slightly lower than no\_bdeni (Table 2), yielding higher export efficiencies (export production / NPP) than no\_bdeni.

Considering the constraints of oxygen, NPP (Fig. 2c, g), and particulate N:P (Table 2), our best solution is calib\_N\*, which is calibrated by the cost function cost\_N\*.

### 3.3 Global patterns of N fluxes

#### 185 3.3.1 Overview of benthic denitrification

Due to the similarity of global benthic denitrification patterns and rates in our calibrated solutions, we show the mean of benthic denitrification from three calibrated solutions (Fig. 3 and Fig. 4j-l). Benthic denitrification rates are highest in highly productive regions over shallow continental shelves (e.g., South and East China Seas, Bering Sea) (Fig. 3a). These areas experience benthic denitrification rates over 100 times greater than deep-ocean sediments.

190 The vertical profile of globally integrated benthic denitrification has a sharp increase in the upper ocean with highest rates on shallow continental shelves (< 160m depth) (Fig. 3b), which accounts for approximately 50% of the total benthic denitrification (Table 2). It should be noted that benthic denitrification is not confined to the upper ocean but occurs at all depths. This is in contrast to water-column denitrification that typically occurs in the upper 900m where oxygen deficient zones develop, and N<sub>2</sub> fixation confined to the euphotic upper 130m in our model (Fig. A1). The average of calibrated solutions predicts the largest  
195 contributions from the sediments in the Pacific and Atlantic Oceans (Fig. 3c).

#### 3.3.2 Influence of benthic denitrification on other N fluxes

The global oceanic fixed-N nitrogen inventory is maintained by balanced supply of N by N<sub>2</sub> fixation at the surface ocean and removal by water-column and benthic denitrification. Figure 4 depicts the global N fluxes of our best model solution calib\_N\* and the flux changes relative to no\_bdeni for each of the three solutions. With the implementation of benthic denitrification,  
200 global N<sub>2</sub> fixation increases, shifting polewards in the Pacific and intensifying in the Atlantic and southern Indian Oceans relative to no\_bdeni. The increased N<sub>2</sub> fixation thereby compensates for the extra N loss due to benthic denitrification in our newly calibrated simulations. With the outward extension of N<sub>2</sub> fixation, however, mild decreases relative to no\_bdeni occur in the centers of the subtropical gyres of the Atlantic and Pacific Oceans.

Water-column denitrification declines relative to no\_bdeni (Table 2). The two new simulations calib\_N\*\_only and calib\_N\*  
205 show very similar changes, with generally strong decreases in the volume of the eastern tropical North Pacific oxygen deficient zone (ODZ) (Fig. 4). Our model does not reproduce the ODZ in the Indian Ocean, hence the absence of water-column denitrification there. Aligned with the lowest global integrated flux of water-column denitrification of calib\_NO<sub>3</sub><sup>-</sup>, water-column denitrification rates are reduced almost everywhere.

We calculate the basin-scale N fluxes shown in Fig. 5 and Table A1. The net fixed-N flux is negative in the Pacific Ocean  
210 and positive in the Atlantic Ocean. Atlantic remains to act as the primary N source for the global ocean, as does no\_bdeni. This is mainly caused by relatively strong iron limitation on diazotrophs in the Pacific Ocean that prevents them balancing the high



denitrification rates there, which becomes alleviated by in North Atlantic Ocean that receives high atmospheric iron input from Saharan dust (Somes et al., 2010a; Landolfi et al., 2013; Weber and Deutsch, 2014).

### 3.4 Spatial distributions of biogeochemical tracers

#### 215 3.4.1 Vertical nutrient distributions

We now compare the vertical distributions of nutrients and oxygen of our newly calibrated simulations to the WOA13 (Garcia et al., 2013a, b) and no\_bdeni, as global averages and for individual ocean basins (Fig. 6). All simulations reproduce the major patterns of the observed climatological vertical distributions of  $\text{NO}_3^-$  and  $\text{PO}_4^{3-}$ , although  $\text{N}^*$  profiles deviate from the WOA13 average the most. This is due to the smaller range of  $\text{N}^*$  ( $-4.5 - 2.5 \text{ mmol/m}^3$ ; Fig. 6c) compared to those of  $\text{NO}_3^-$  ( $0 - 40$   
220  $\text{mmol/m}^3$ ; Fig. 6a) and  $16 \times \text{PO}_4^{3-}$  ( $0 - 48 \text{ mmol/m}^3$ ; Fig. 6b). The simulation no\_bdeni underestimates  $\text{N}^*$  in the upper 1000 meters, whereas the simulations including benthic denitrification and calibrated to  $\text{N}^*$  (i.e. calib\_N\*\_only, calib\_N\*) better reproduce upper-ocean  $\text{N}^*$  where N cycle fluxes are strongest. In the deep ocean (below 1000m), due to the addition of benthic denitrification, both calib\_N\*\_only and calib\_N\* depart more from the observation than no\_bdeni, especially in the Pacific and Southern Oceans suggesting that benthic denitrification is overestimated there. The greatest deviation of the  $\text{N}^*$   
225 profiles, particularly in the deep ocean, occurs in calib\_NO $_3^-$ .

Profiles of  $\text{N}^*$  result from the vertical distributions of the processes affecting  $\text{N}^*$ , and the impact of ocean circulation. Denitrification occurs in both the water column and the sediments and imparts a negative signature to  $\text{N}^*$ , whereas  $\text{N}_2$  fixation imparts a positive signature to  $\text{N}^*$  in the upper ocean. Our calibrated solutions with benthic denitrification yield higher  $\text{N}_2$  fixation in the euphotic zone and lower water-column denitrification in oxygen-deficient zones (ODZs) compared to no\_bdeni,  
230 both of which contribute to increasing upper ocean  $\text{N}^*$  compared to no\_bdeni, thereby better reproducing observed  $\text{N}^*$  profiles. However, benthic denitrification also occurs at high rates in the upper ocean on the continental shelves, which can compensate the  $\text{N}^*$  effects of  $\text{N}_2$  fixation and lead to reduced  $\text{N}^*$  relative to no\_bdeni in the shallow subsurface ocean (e.g., calib\_N\*\_only in the Atlantic and Indian Oceans). The low vertical  $\text{N}^*$  variability in the Indian Ocean from 200 to 1000m is due to the lack of an ODZ and subsequent water-column denitrification. This is partially counteracted by high benthic denitrification in the  
235 upper 200m, causing an upper-ocean  $\text{N}^*$  gradient inconsistent with observations. In order to disentangle the individual effects, we also show the horizontal distribution of  $\text{N}^*$ , which will be addressed in Section 3.4.2.

For  $\text{O}_2$ , all model simulations slightly overestimate global-averaged deep ocean  $\text{O}_2$ , although the vertical patterns are generally consistent with observations. The positive bias in the Southern Ocean (SO) occurs in intermediate layers (300–2500m). Indian Ocean Deep Water (IODW, 1400–3500m) deviations relative to observations has been partly attributed to the overesti-  
240 mation of  $\text{O}_2$  in SO (Schmidt et al., 2021), as Circumpolar Deep Water (CDW) is the origin of IODW.

Global  $\text{O}_2$  profiles of our new simulations show increased concentrations relative to no\_bdeni in the mesopelagic zone (200–1000m), where the distribution of  $\text{O}_2$  is largely dominated by the remineralization of particulate organic matter (POM). This is likely caused by slightly decreased global export production described above (Table 2).  $\text{O}_2$  concentrations in the upper 1000 meters are lower in calib\_N\* and calib\_N\*\_only than in calib\_NO $_3^-$ . This may be explained by the higher calibrated



245 remineralization rates ( $\nu_{\text{det}}$ ) when the model is constrained with  $N^*$  (either `calib_N*` or `calib_N*_only`) compared to when  
constrained with  $\text{NO}_3^-$  (Table 1). Notably, the vertical  $\text{O}_2$  profiles of `calib_N*_only` are in close proximity to the observations,  
implying that  $N^*$  alone sufficiently constrains the distribution of  $\text{O}_2$  in our model. As both water-column and benthic deni-  
trification are tightly linked to oxygen, a proper representation of the  $N^*$  distribution requires a realistic reproduction of the  
oxygen distribution in the model that resolves major marine biogeochemical processes properly.

### 250 3.4.2 Lateral distribution of $N^*$

Examining the horizontal distribution of  $N^*$  at the surface allows us to disentangle the local and regional responses of  $N^*$   
to  $\text{N}_2$  fixation and benthic denitrification. The inclusion of benthic denitrification considerably improves the reproduction of  
observed near-surface (50m)  $N^*$  in the North Pacific Subpolar Gyre (Fig. 7c), which is largely occupied by shallow continental  
shelves extending into the Okhotsk and Bering Seas (Fig. 3a). Likewise, near-surface  $N^*$  in the Arctic ocean is lower than in  
255 `no_bdeni`, more in line with the observations (Fig. 7a-c). Here, however, this improvement is limited, likely due to the coarse  
resolution. Our model lacks of representation of narrow continental shelves (e.g., among Canadian Arctic archipelago islands)  
and circulation around them.

The twilight zone collects euphotic zone signals through sinking and remineralization of organic matter. Thus, the non-  
Redfield stoichiometry of the exported organic matter, local denitrification in both the water column and the sediments, as well  
260 as  $\text{N}_2$  fixation all contribute to the horizontal pattern of  $N^*$  at 300 m. The low  $N^*$  signal originating from excessive water-  
column denitrification at 300m in `no_bdeni` is mitigated in the the eastern tropical north Pacific ODZ and nearly gone in the  
the eastern tropical south Pacific ODZ in the new simulations (Fig. 4). The optimal model solutions better simulate elevated  
 $N^*$  in the Atlantic Ocean, Indian Ocean, and Western North Pacific (e.g., see `calib_N*` in Fig. 7f). This is due to the higher  
contribution of  $\text{N}_2$  fixation in these regions (Fig. 4) relative to `no_bdeni`, but also to the elevated euphotic phytoplankton and  
265 associated detritus N:P (not shown) with the assumption of identical remineralization rates of detrital N and P. Compared to the  
observations, our model underestimates  $N^*$  in the western and central parts of the South Pacific subtropical gyre. This signal is  
driven both by underestimated  $\text{N}_2$  fixation rates (Fig. 4a) and low N:P ratios of phytoplankton and corresponding detritus N:P  
( $<13.5$ ) compared to the Redfield ratio (molar N:P = 16) that is applied in the calculation of  $N^*$ .

The influence of local biogeochemical processes, such as benthic denitrification, on  $N^*$  is scarcely discernible at 2000m. The  
270 distribution of  $N^*$  in the deep ocean reflects global biogeochemical signals accumulating over decades to millennia along the  
thermohaline circulation (Fripiat et al., 2021; DeVries and Primeau, 2011), thus diluting the local flux signals. Our simulations  
constrained by  $N^*$  (`calib_N*_only` and `calib_N*`) reproduce the basin gradient visible in the WOA 2013 data best (see `calib_N*`  
in Fig. 7h).

### 3.4.3 Patterns of $\text{O}_2$

275 In the core of the ODZs ( $\approx 300\text{m}$ ), the  $\text{O}_2$  distribution varies similarly across all calibrated new simulations compared to  
`no_bdeni` (not shown). Low- and mid-latitude oceans have higher subsurface oxygen concentrations (Fig. 8), resulting in less  
intense ODZs and water-column denitrification (Fig. 4). The simulated and observed spatial patterns are broadly comparable,



with the exception of the Arabian Sea, where the observations reveal the presence of a perennial ODZ (Fig. 8a). This implies that including benthic denitrification may improve the representation of ODZs in global ocean biogeochemical models that typically overestimate their volume (Cabr e et al., 2015).

The overestimation of  $O_2$  in calib\_N\* compared to WOA13 at 2000m occurs mainly in the Pacific Ocean and the change relative to no\_bdeni at this depth is spatially homogeneous. While our model solutions show consistent changes in  $O_2$  concentration relative to no\_bdeni that broadly point towards better agreement with observations at 300m, changes often are in a direction diverging from observations at 2000m (not shown). This finding is also reflected in the vertical profiles of globally averaged  $O_2$  shown above (Fig. 6).

### 3.5 Global patterns of C fluxes

Our definition of global NPP includes the sum of phytoplankton NPP and diazotroph NPP. Export production (EP) is calculated as the product of the biomass of sinking particles and their sinking speed at 130m depth. These sinking particles consist of detritus derived from phytoplankton, diazotrophs, and zooplankton. High production occurs in equatorial and subpolar regions (Fig. 9a, e), with the highest NPP found in the equatorial oceans. In contrast, EP in equatorial and subpolar oceans are comparable. The low export efficiency (EP/NPP) of equatorial oceans result from elevated particle decomposition rates in high-temperature environments, owing to both increasing zooplankton respiration and detritus remineralization with temperature in our model.

Compared to no\_bdeni, the new simulations exhibit notable decreases of NPP, mainly located in and adjacent to these high-production regions (Fig. 9b-d). While the primary pattern observed in the distribution of EP is a decline in most areas, there are some small areas that contain an increase (Fig. 9f-h). The decline in EP results in elevated concentrations of oxygen in the underlying subsurface ocean (Fig. 8c). Among the three solutions, calib\_N\* and calib\_N\*\_only exhibit more similar patterns with each other than with calib\_NO<sub>3</sub><sup>-</sup>.

## 4 Model and calibration limitations

In the northern Indian Ocean, our model shows a too low N\* signal due to benthic denitrification at the Bay of Bengal, whereas the WOA13 data indicates an intense ODZ and robust water-column denitrification in the Arabian Sea (Fig. 7d). This is likely due to underestimated coastal upwelling by the coarse model resolution in the Arabian Sea. An examination of CMIP5 models also reveals the presence of systematic deficiencies in the oceanic physics of these Earth System Models (ESMs), resulting in an inaccurate representation of the east-west  $O_2$  gradient in the northern Indian Ocean (Schmidt et al., 2021). The absence of a persistent ODZ in the Arabian in our model is likely a reason why our global water-column denitrification and  $N_2$  fixation rates are on the low-end of observational estimates.

The absence of an Arabian Sea ODZ may also be affected by the biome resolution of our calibration method, which has only one biome for the entire Indian Ocean, filtering out sub-basin variability. Sub-dividing the Indian Ocean biome might have the potential to improve the ability of the cost function to constrain  $O_2$  and water-column denitrification. Future research building





310 on high-resolution earth system models may be amenable to choose a spatially finer calibration in terms of 56 biogeochemical provinces (Longhurst, 2007). Concerning the unique characteristic of  $O_2$  among tracers, an additional improvement would be to assume a normal distribution of  $O_2$  concentration in the global ocean, which represents the data in WOA13 better than the log-normal distribution used here. However, since `calib_N*_only` chosen by `cost_N*` without calibrating against  $O_2$  fails to reproduce the intense water-column denitrification in the North Indian Ocean as well, further investigation is required.

315 The vertical distribution of  $N^*$  shows that simulated  $N^*$  tends to underestimate the observed  $N^*$  at depth, particularly below 1000m (Fig. 6c). There are some promising developments that could be implemented to improve the deep-ocean  $N^*$  distribution. Our cost function metrics tend to focus on the upper ocean by including seasonal-scale variability only for the upper 550m. This artificial emphasis on the upper ocean would be balanced by a refined volume-weighted cost function. In the current model configuration, the sinking velocity increases linearly with depth all the way to the ocean floor, which may lead  
320 to an overestimation of benthic denitrification in the deep ocean. A linear increase only up to 1000 meters (Lam and Marchal, 2015) could give us a better representation of global carbon fluxes and corresponding benthic denitrification rates, which is the only plausible nitrogen loss flux that could occur below 1000m (Fig. A1). Likewise, incorporating dissolved organic matter dynamics or preferential remineralization of phosphorus could assist in the reproduction of vertical gradients of  $N^*$  (Somes and Oschlies, 2015). Improvements to the upper ocean may also have the potential to improve the deep-ocean performance,  
325 such as including  $w_{d0}$  into the calibrated parameters. By taking both  $w_{d0}$  (particle sinking velocity at the surface ocean) and  $w_{dd}$  into account for the calibration, the particle flux profile in our model could possibly be represented more accurately.

The influence of particle fluxes on  $N^*$  via the effect on benthic denitrification leads to a further discussion of the model uncertainties in the representation of benthic denitrification. A first uncertainty in the model estimate of benthic denitrification via the parameterization employed results from the uncertainties in the simulated bottom-water  $O_2$  and  $NO_3^-$  concentrations and  
330 the organic carbon rain rate. The accurate simulation of the rain rate is one of the most critical issues in ocean biogeochemistry and is associated with a high uncertainty (Clements et al., 2022; Kiko et al., 2017). A promising option could be to resolve the dependency of remineralization rate on  $O_2$ , which could contribute to an accurate representation of the unique vertical profiles observed in ODZs (Pavia et al., 2019; Engel et al., 2022). Such efforts are necessary for a proper investigation of the relation between benthic denitrification and water-column denitrification. Moreover, the empirically-derived parameterization  
335 of benthic denitrification itself is subject to a certain uncertainty, albeit to a lesser extent (Bohlen et al., 2012). Ocean physics introduces additional uncertainty. For example, the low physical resolution of the existing UVic model framework imposes relatively little computational demand, but the representation of N and C fluxes could benefit from a higher spatial resolution.

## 5 Conclusion

In order to explore the sensitivity to prior assumptions, we applied our cost function to calibrate model solutions against three  
340 different combinations of observations. The best model solution `calib_N*` reaches the lowest cost function with input of Chl,  $PO_4^{3-}$ ,  $O_2$  and  $N^* = NO_3^- - 16PO_4^{3-} + 2.9$ . Model solution `calib_N*_only` shows significant parallels with `calib_N*` in various biogeochemical fluxes and tracers. Compared with the canonical cost function `cost_NO_3^-`, that calibrates the model against Chl,





345  $\text{PO}_4^{3-}$ ,  $\text{O}_2$  and  $\text{NO}_3^-$ , as was done previously (Pahlow et al., 2020; Chien et al., 2020), including  $\text{N}^*$  provide better constraints on globally averaged  $\text{N}^*$  and nitrate, and also on globally integrated water-column denitrification and thus  $\text{N}_2$  fixation. The greater constraining capacity of  $\text{N}^*$  in comparison to considering nitrate and phosphate separately highlights the importance of accounting for correlations among variables within the cost function (Krishna et al., 2019) and demonstrates the power of diagnostic tracers such as  $\text{N}^*$  for diagnostic studies of the ocean nitrogen cycle (DeVries et al., 2013; Eugster and Gruber, 2012; Deutsch et al., 2007).

350 UVic-OPEM achieves a better representation of  $\text{N}_2$  fixation and  $\text{N}^*$  by incorporating benthic denitrification. Our model configurations demonstrate higher estimates of global  $\text{N}_2$  fixation and an extension of  $\text{N}_2$  fixation to higher latitudes in the Pacific, Atlantic and Indian Oceans compared to the simulation excluding benthic denitrification (no\_bdeni). The calibrated model solutions calib\_ $\text{N}^*$  and calib\_ $\text{N}^*$ \_only yield a global  $\text{N}_2$  fixation of 137.7 and 136.1  $\text{Tg N yr}^{-1}$  respectively. The most apparent improvements of modelled  $\text{N}^*$  distribution compared to WOA13 (Garcia et al., 2013a) are located in the surface layers of the North Pacific subpolar gyre, where consistently low  $\text{N}^*$  signals result from the newly-added benthic denitrification in  
355 the absence of local changes from other N fluxes and transfers. The improved representation of the global nitrogen cycle enables a more precise reproduction of net primary productivity. The estimated global integrated NPP, ranging from 52.8 to 63.0  $\text{Pg C yr}^{-1}$ , is consistent with the estimates derived from satellite and Argo-float observations (Silsbe et al., 2016; Johnson and Bif, 2021). The most significant decrease in NPP occurs in the tropical oceans, with a concomitant contraction of oxygen-deficient zones (ODZs). Benthic denitrification plays a globally important role shaping  $\text{N}_2$  fixation and NPP throughout the  
360 global ocean and should be considered in marine biogeochemical models when trying to understand and predict changes in  $\text{N}_2$  fixation and marine C fluxes.



**Table 1.** Parameter names, ranges, unites and descriptions.

Symbol	Range	Reference range	calib_NO <sub>3</sub> <sup>-</sup>	calib_N*_only	calib_N*	Reference (no_bdeni)	Definition and units
$A_{0,phy}$	200–400	120–280	365	339	205	229	phytoplankton pot. nutr. affinity ( $m^3 molC^{-1}d^{-1}$ )
$A_{0,dia}$	200–400	—	311	383	321	171	diazotroph pot. nutrient affinity ( $m^3 molC^{-1}d^{-1}$ )
						( $= 0.75 \times A_{0,phy}$ )	
$\alpha_{phy}$	0.4–0.6	—	0.52	0.40	0.40	0.4	phytoplankton pot. light affinity ( $m^2W^{-1}molC gChl^{-1}d^{-1}$ )
$\alpha_{dia}$	0.4–0.6	—	0.51	0.47	0.58	0.5	diazotroph potential light affinity ( $m^2W^{-1}molC gChl^{-1}d^{-1}$ )
$Q_{0,phy}^N$	0.04–0.06	0.04–0.06	0.05282	0.05396	0.05879	0.04128	phytoplankton subsistence N quota ( $mol molC^{-1}$ )
$Q_{0,dia}^N$	0.10–0.16	0.06–0.12	0.1089	0.1246	0.1231	0.067	diazotroph subsistence N quota ( $mol molC^{-1}$ )
$Q_{0,phy}^P$	2–4	1.3–2.3	2.1	2.2	2.6	2.2	phytoplankton subsistence P quota ( $mmol molC^{-1}$ )
$Q_{0,dia}^P$	2–4	2.5–3.5	2.56	2.08	3.58	2.71	diazotroph subsistence P quota ( $mmol molC^{-1}$ )
$k_{Fe,phy}$	0.04–0.08	0.04–0.08	0.079	0.042	0.040	0.066	phytoplankton half-satur. const. for Fe ( $\mu mol m^{-3}$ )
$k_{Fe,dia}$	0.08–0.12	—	0.093	0.118	0.119	0.132	diazotroph half-satur. const. for Fe ( $\mu mol m^{-3}$ )
						( $= 2 \times k_{Fe,phy}$ )	
$g_{max}$	1–2	1–2	1.82	1.47	1.26	1.75	zooplankton max. specific ingestion rate ( $d^{-1}$ )
$\phi_{phy}$	100–200	100–200	178	146	145	118	capture coefficient of phytoplankton ( $m^3 molC^{-1}$ )
$\phi_{dia}$	150–250	150–250	215	202	232	232	capture coefficient of diazotroph ( $m^3 molC^{-1}$ )
$\phi_{det}$	20–100	20–100	43	72	92	94	capture coefficient of detritus ( $m^3 molC^{-1}$ )
$\phi_{zoo}$	100–200	100–200	118	149	156	118	capture coefficient of zooplankton ( $m^3 molC^{-1}$ )
$\lambda_{0,phy}$	0.01–0.03	0.01–0.03	0.016	0.016	0.014	0.018	T-dependent leakage of phytoplankton ( $d^{-1}$ ) $= M_{0,dia}$ : diazotroph T-dependent mortality rate
$w_{dd}$	0.03–0.06	—	0.0387	0.0391	0.0568	0.06	linear increase of sinking speed with depth ( $m^{-1}$ )
$\nu_{det}$	0.04–0.09	0.04–0.09	0.058	0.073	0.080	0.087	remineralsation rate at 0°C ( $d^{-1}$ )
$M_{0,phy}$	—	—	0.03	0.03	0.03	0.03	phytoplankton T-independent mortality rate ( $d^{-1}$ )
$\lambda_{0,dia}$	—	—	0	0	0	0	diazotroph T-independent leakage rate ( $d^{-1}$ )

no\_bdeni refers to OPEM\_H in Pahlow et al. (2020); Chien et al. (2020).



**Table 2.** Tracers, fluxes, and costs of OPEM simulations.

variable	model configuration				units or input variables
	no_bdeni	calib_NO <sub>3</sub> <sup>-</sup>	calib_N*_only	calib_N*	
average NO <sub>3</sub> <sup>-</sup>	31.3	29.3	30.5	30.4	mmol m <sup>-3</sup>
average O <sub>2</sub>	188	195.7	194.2	183.5	mmol m <sup>-3</sup>
average N*	-1.17	-2.55	-1.27	-1.44	mmol m <sup>-3</sup>
average particulate N:P	15.49	16.15	16.42	16.15	mol mol <sup>-1</sup>
N <sub>2</sub> fixation	69.5	95.5	136.1	137.7	Tg N yr <sup>-1</sup>
Water-column Deni. (W)	69.5	2.8	42.4	30.3	Tg N yr <sup>-1</sup>
Benthic Deni. (B)	0	91.4	94.4	105.5	Tg N yr <sup>-1</sup>
B/W	–	32.6	2.2	3.5	1
NPP	88	52.8	63.0	59.3	Pg C yr <sup>-1</sup>
Export production (at 130m)	4.7	3.4	4.0	4.2	Pg C yr <sup>-1</sup>
B <sub>continental_shelf</sub> /B	–	0.5	0.6	0.5	1
cost_NO <sub>3</sub> <sup>-</sup>	187.2	165	202	222	NO <sub>3</sub> <sup>-</sup> , PO <sub>4</sub> <sup>3-</sup> , O <sub>2</sub> , Chl
rank	4 <sup>†</sup>	<b>1</b>	20	30	
cost_N*_only	–	37.1	16.7	18.1	N*
rank	–	32	<b>1</b>	3	
cost_N*	–	118.9	79.1	77.3	N*, PO <sub>4</sub> <sup>3-</sup> , O <sub>2</sub> , Chl
rank	–	41	3	<b>1</b>	

<sup>†</sup> no\_bdeni is the 4th best solution among the 400 simulations conducted without benthic denitrification in the previous studies (Pahlow et al., 2020; Chien et al., 2020). All other rank numbers refer to the positions among the newly generated 600 simulations that incorporate benthic denitrification. cost\_NO<sub>3</sub><sup>-</sup> in this study is the same as the cost function in the previous studies.

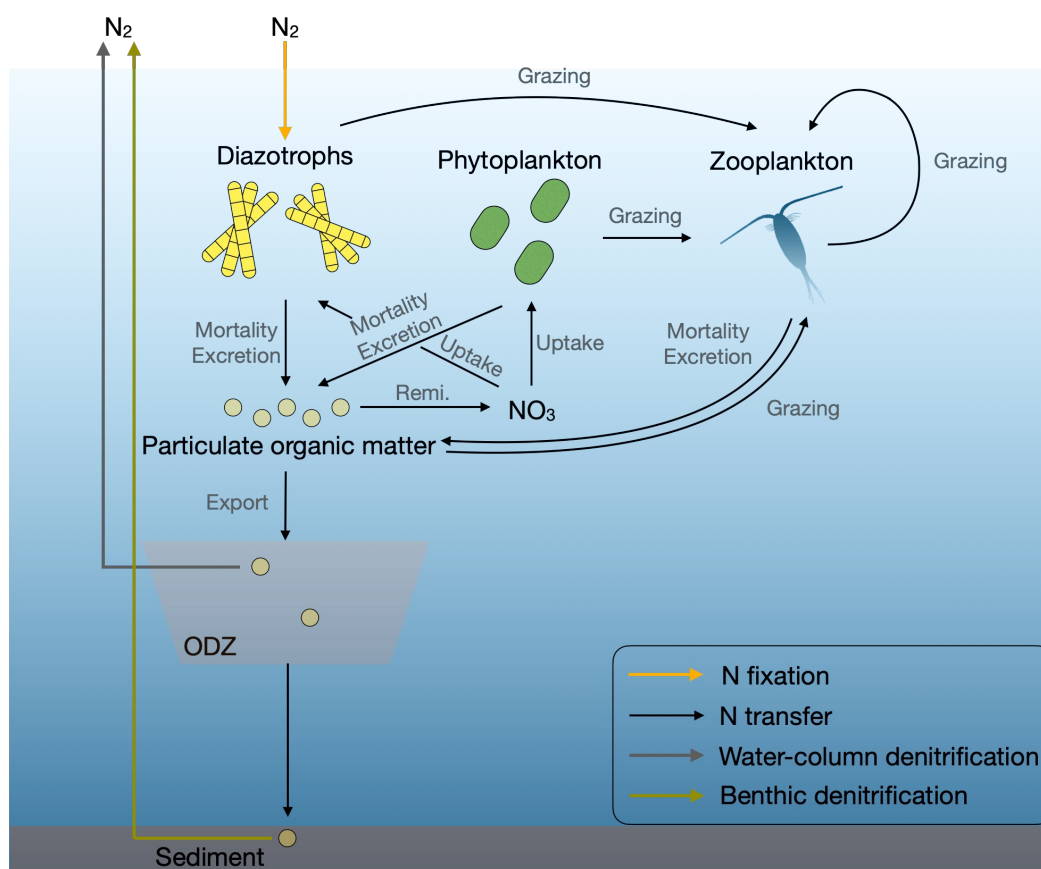


**Figure 1.** Marine N flows in our model. Remi. = remineralization. ODZ = oxygen deficient zone.

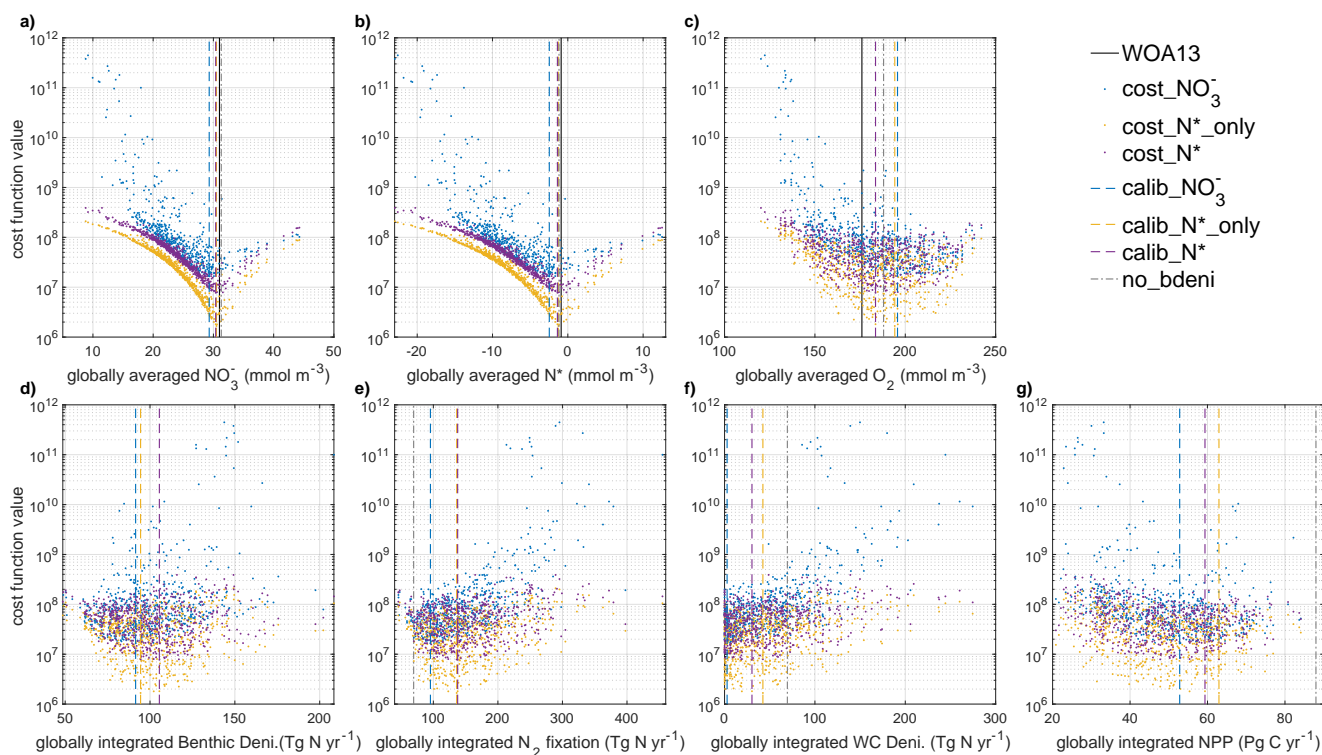


**Figure 2.** Relations between global averages of tracers, integral of fluxes and cost function values. The x-axis of each panel displays the ranges of (a)  $\text{NO}_3^-$ , (b)  $\text{N}^*$ , (c)  $\text{O}_2$  and (d) benthic denitrification, (e)  $\text{N}_2$  fixation, (f) water-column denitrification, (g) NPP of our ensemble simulations. The calibrated solutions are displayed as dashed lines with colors that correspond to their respective cost functions ( $\text{cost\_NO}_3^-$ ,  $\text{cost\_N}^*\_\text{only}$ ,  $\text{cost\_N}^*$ ). In order to compare, we also depict the values of tracers from WOA13 data (Garcia et al., 2013a, b) with solid black lines, whereas the tracers and fluxes from the simulation no\_bdeni with dash-dotted grey lines. Deni. is short for denitrification and WC. for water-column.

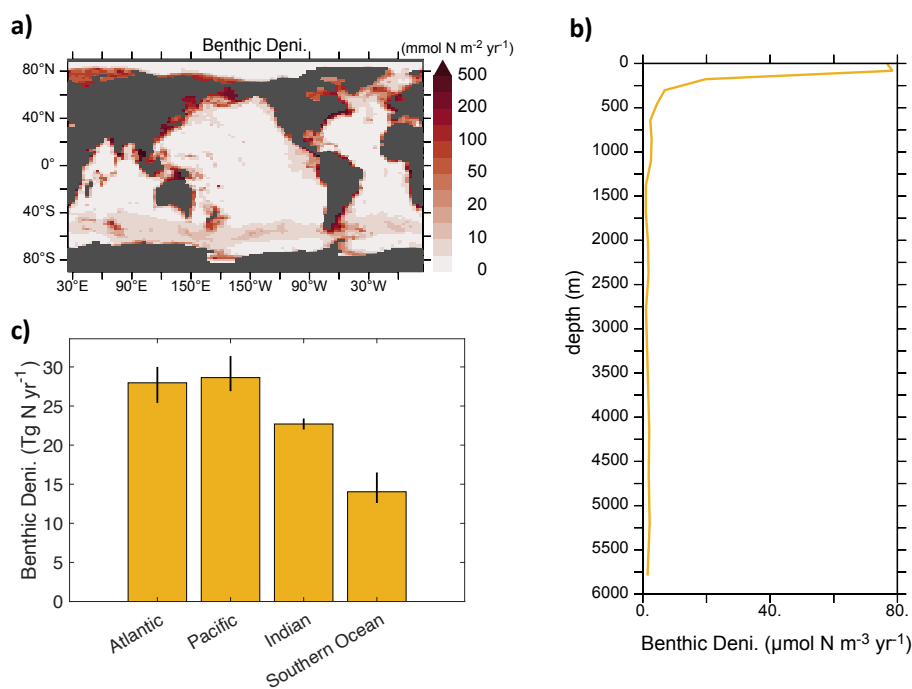


**Figure 3.** Spatial distributions of benthic denitrification, based on the mean values obtained from our calibrated solutions. (a) Geographic distribution of the vertical integrals. (b) Vertical profile of the global averages. (c) Four ocean basin integrals. Southern Ocean is defined as the body of water located to the south of the 40°S latitude. The error bar in panel (c) indicates the uncertainty window among the calibrated solutions (i.e.,  $\text{calib\_NO}_3^-$ ,  $\text{calib\_N}^*$ \_only and  $\text{calib\_N}^*$ ).

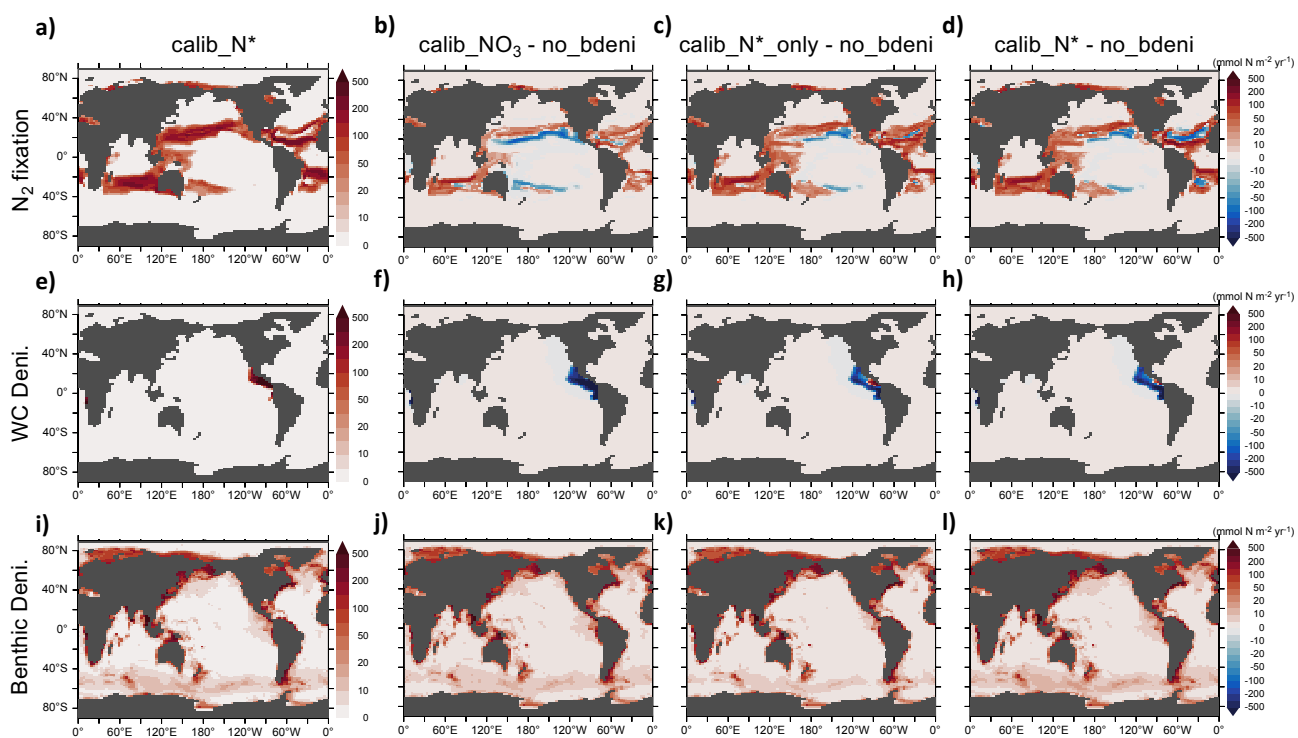


**Figure 4.** N<sub>2</sub> fixation, water-column denitrification and benthic denitrification distributions of calib\_N\* and the changes of three new solutions relative to no\_bdeni.



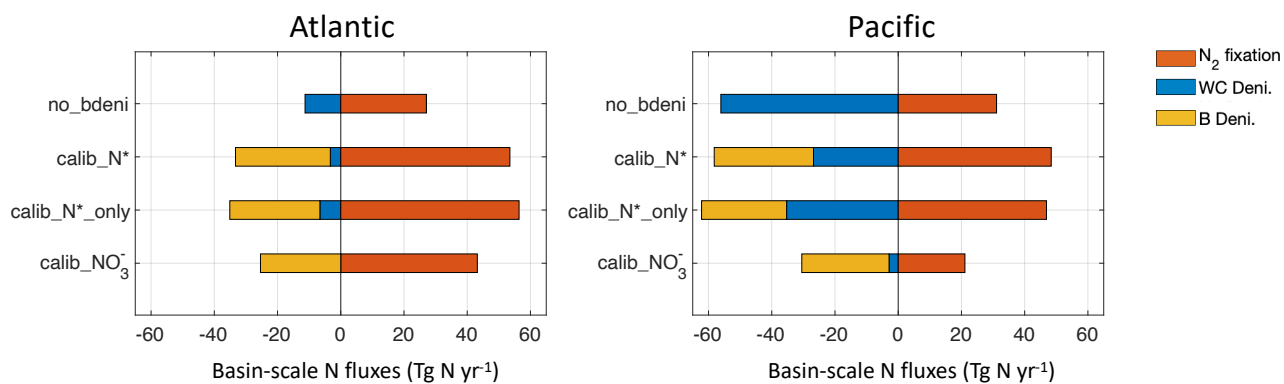


**Figure 5.** Basin-scale bio-available N fluxes in the Atlantic and Pacific oceans, including N<sub>2</sub> fixation, water-column denitrification and benthic denitrification.

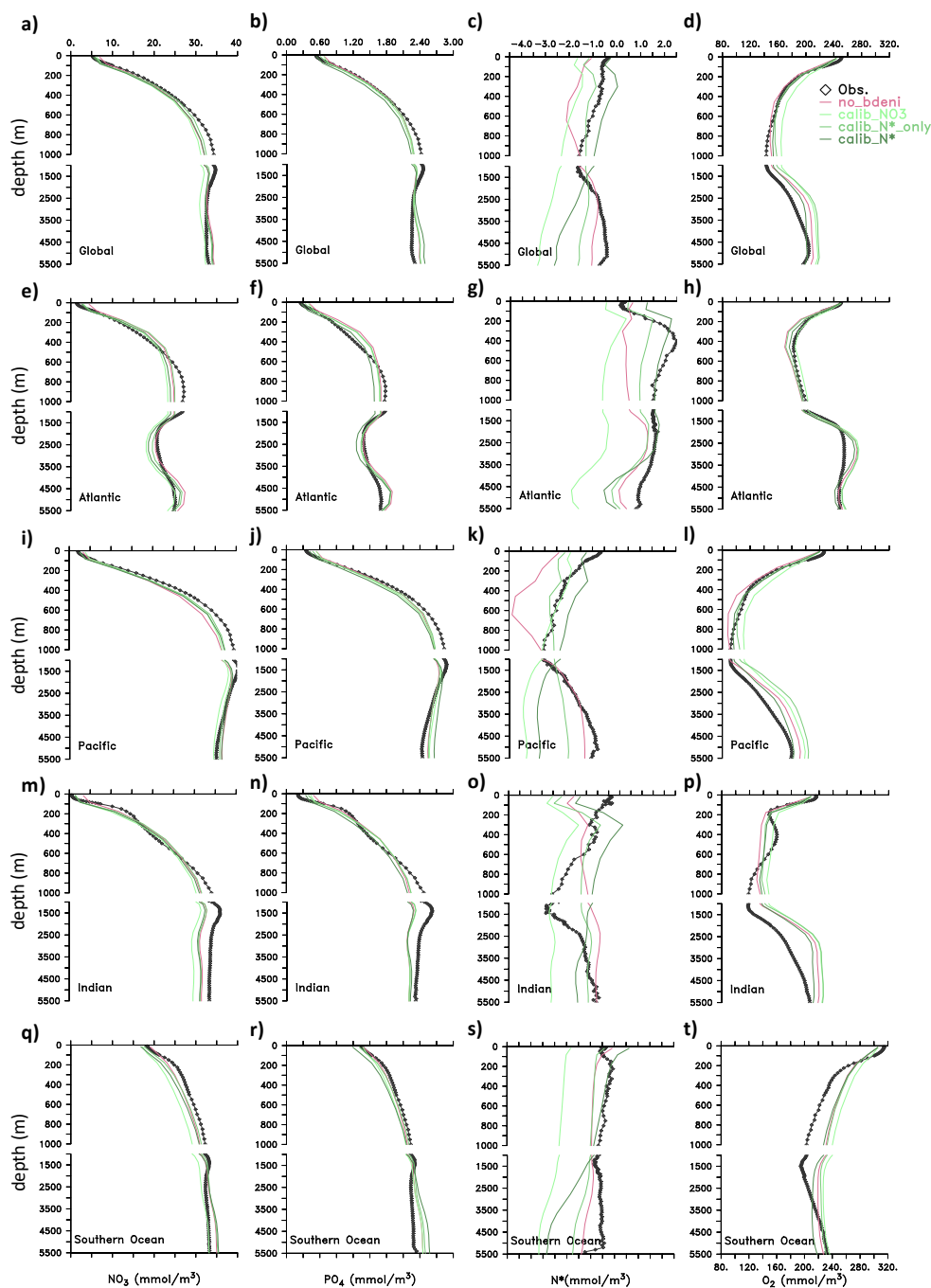


**Figure 6.** Vertical distributions of tracers ( $\text{NO}_3^-$ ,  $\text{PO}_4^{3-}$ ,  $\text{N}^*$ ,  $\text{O}_2$ ) in global and respect basins (Atlantic, Pacific, Indian, Southern Oceans).

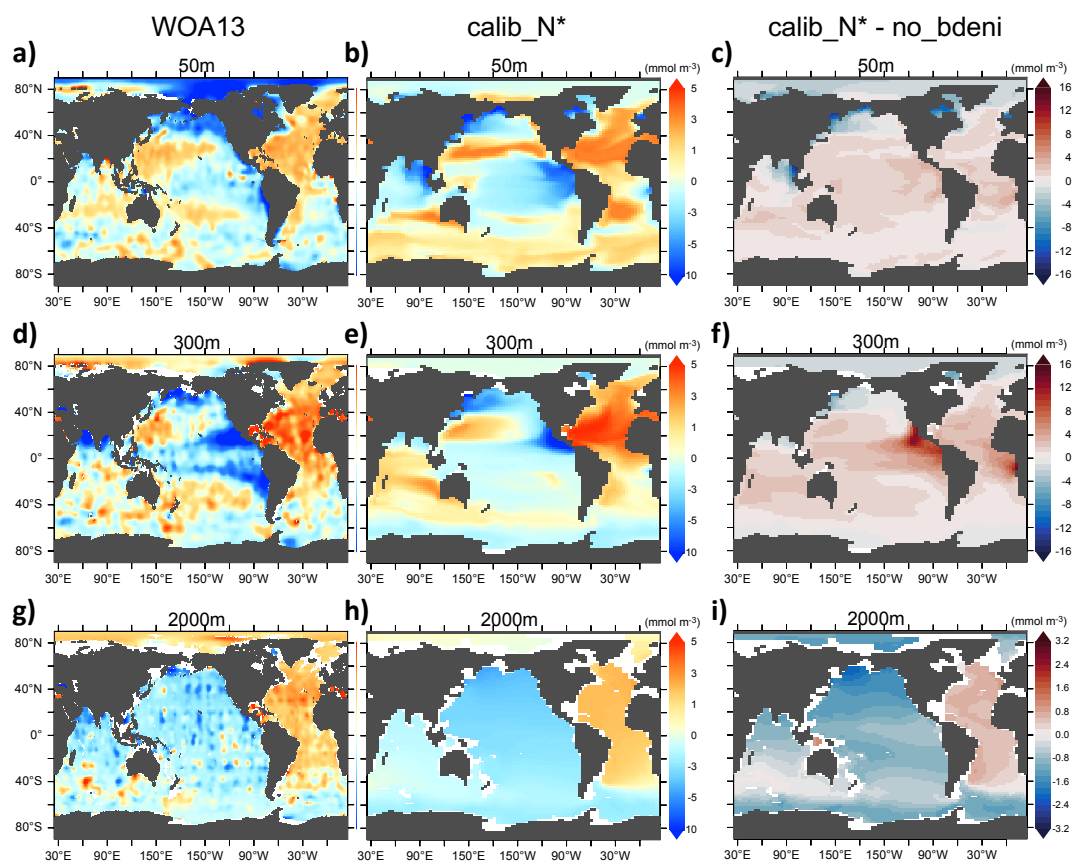


**Figure 7.** Spatial distribution of N\* (50m, 300m, 2000m) for WOA13 and one of our calibrated solutions calib\_N\*, as well as changes in this calibrated solution compared to no\_bdeni.

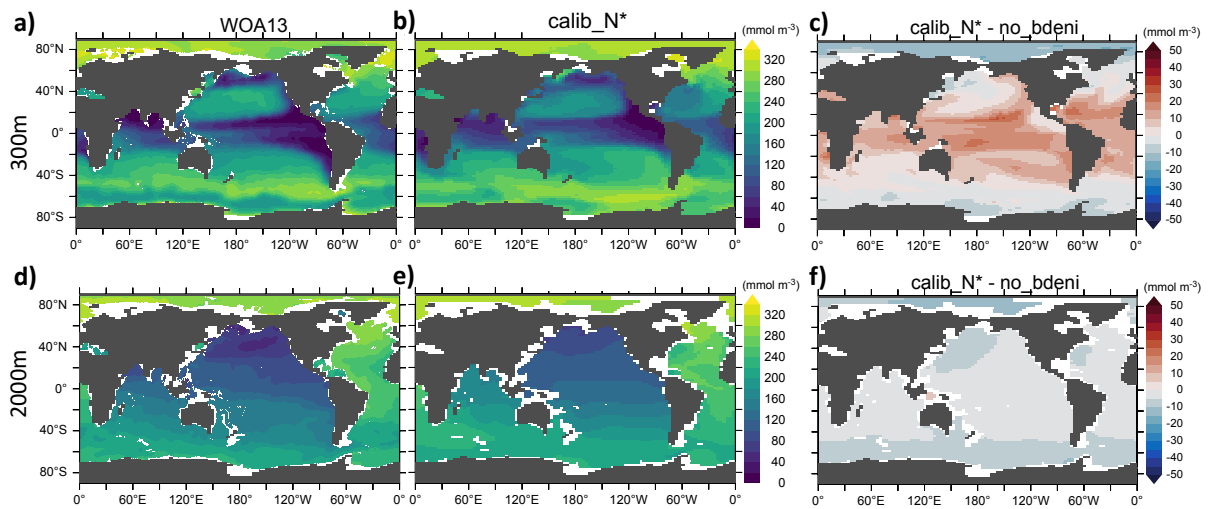


**Figure 8.** Spatial distribution of oxygen concentration at 300m and 2000m for calib\_N\* and the changes of three new solutions relative to no\_bdeni.

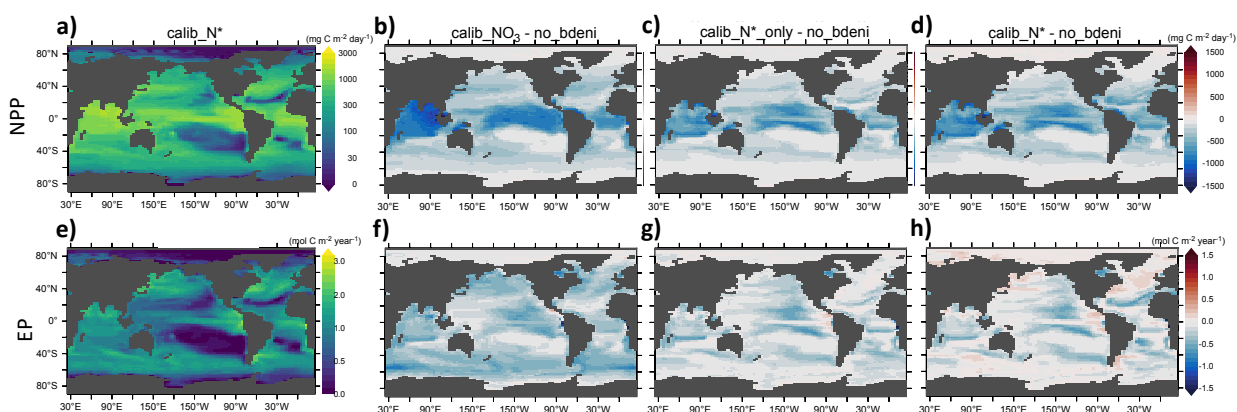


**Figure 9.** Vertically-integrated net primary production (NPP) and export production (EP) distributions at 130m for calib\_N\* and the changes of three new solutions relative to no\_bdeni.

*Code and data availability.* The University of Victoria Earth System Climate Model version 2.9 is available at <https://terra.seos.uvic.ca/model/> (last access: 22 November 2023) ("updated model" version). The benthic-denitrification-included model and OPEM codes, Matlab scripts of cost function, and data shown in the figures and used for this paper are available at <https://doi.org/10.5281/zenodo.10469908>.

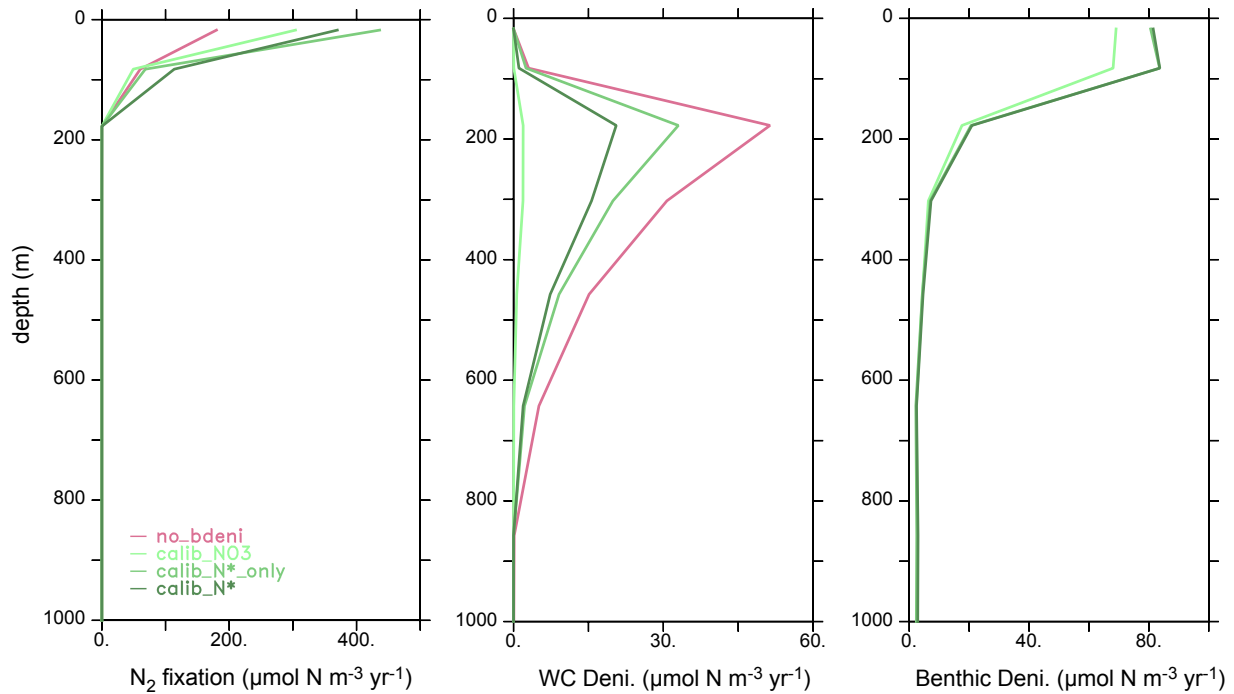


**Figure A1.** Vertical profiles of the global averages of major N fluxes at upper 1000m.



**Table A1.** vertically integrated N fluxes, excess N relative to P in the organic matter, and average total excess N relative to P including organic and inorganic forms for ocean basins

	Atlantic	Pacific	Indian	SO		Atlantic	Pacific	Indian	SO	
		d2_6								
N <sub>2</sub> Fixation	43.2	21.1	24.3	0						
WC Deni	0	2.9	0	0						
B Deni	25.4	27.6	22	13.0						
Net	17.7	-9.4	2.3	-13						
PON*	309.3	12.3	16.1	11.9						
$\overline{TN^*}$	-1.1	-3.3	-2.5	-2.6						
		f2_12								
N <sub>2</sub> Fixation	56.4	46.9	31.9	0						
WC Deni	6.6	35.3	0.2	0						
B Deni	28.5	26.9	22.7	12.6						
Net	21.3	-15.3	9.0	-12.6						
PON*	522.9	-151.8	69.7	-21.2						
$\overline{TN^*}$	0.5	-2.2	-1.0	-1.2						
		b2_4								
N <sub>2</sub> Fixation	53.5	48.4	34.2	0						
WC Deni	3.3	26.8	0	0						
B Deni	30	31.4	23.4	16.5						
Net	20.2	-9.8	10.8	-16.5						
PON*	548.5	-18.7	147.4	-279.6						
$\overline{TN^*}$	0.7	-2.6	-1.1	-1.5						
		no_bdeni								
N <sub>2</sub> Fixation						27.1	31.1	11.0	0.0	
WC Deni						11.3	56.1	0	0	
Net						15.7	-25.0	10.9	0.0	
PON*						104.4	-416.1	53.2	-269.3	
$\overline{TN^*}$						0.4	-2.0	-0.8	-1.0	

where  $PON^* = PON - 16 * POP$  and  $TN^* = (PON + NO_3^-) - 16 * (POP + PO_4^{3-}) + 2.9 = N^* + PON^*$ .

The unit for fluxes is  $TgNy r^{-1}$  and that of the vertically-integrated  $PON^*$  is  $10^{12} mmol m^{-3}$ .

*Author contributions.* C.J.S., A.L. and M.P. designed the study. N.L., C.C. and M.P. carried out the simulations and calibration. N.L. conducted the analysis. All authors discussed the results and wrote the manuscript.

*Competing interests.* The authors declare no competing financial interest.



<https://doi.org/10.5194/egusphere-2024-123>  
Preprint. Discussion started: 18 January 2024  
© Author(s) 2024. CC BY 4.0 License.



*Acknowledgements.* N.L. was supported by the the China Scholarship Council (CSC; grant no. 201906330071). C.J.S. was supported by the  
370 Deutsche Forschungsgemeinschaft (DFG project number 445549720).



## References

- Bohlen, L., Dale, A. W., and Wallmann, K.: Simple transfer functions for calculating benthic fixed nitrogen losses and C:N:P regeneration ratios in global biogeochemical models, *Global Biogeochemical Cycles*, 26, 2012.
- Bopp, L., Aumont, O., Kwiatkowski, L., Clerc, C., Dupont, L., Ethé, C., Gorgues, T., Sférian, R., and Tagliabue, A.: Diazotrophy as a key driver of the response of marine net primary productivity to climate change, *Biogeosciences*, 19, 4267–4285, 2022.
- 375 Brandes, J. A. and Devol, A. H.: A global marine-fixed nitrogen isotopic budget: Implications for Holocene nitrogen cycling, *Global Biogeochem. Cycles*, 16, 67–1–67–14, 2002.
- Cabré, A., Marinov, I., Bernardello, R., and Bianchi, D.: Oxygen minimum zones in the tropical Pacific across CMIP5 models: mean state differences and climate change trends, *Biogeosciences*, 12, 5429–5454, 2015.
- 380 Chien, C.-T., Pahlow, M., Schartau, M., and Oschlies, A.: Optimality-based non-Redfield plankton–ecosystem model (OPEM v1.1) in UVic-ESCM 2.9 – Part 2: Sensitivity analysis and model calibration, *Geosci. Model Dev.*, 13, 4691–4712, 2020.
- Clements, D. J., Yang, S., Weber, T., McDonnell, A. M. P., Kiko, R., Stemmann, L., and Bianchi, D.: Constraining the particle size distribution of large marine particles in the global ocean with *in situ* optical observations and supervised learning, *Global Biogeochem. Cycles*, 36, 2022.
- 385 Deutsch, C., Sarmiento, J. L., Sigman, D. M., Gruber, N., and Dunne, J. P.: Spatial coupling of nitrogen inputs and losses in the ocean, *Nature*, 445, 163–167, 2007.
- DeVries, T. and Primeau, F.: Dynamically and Observationally Constrained Estimates of Water-Mass Distributions and Ages in the Global Ocean, *J. Phys. Oceanogr.*, 41, 2381–2401, 2011.
- DeVries, T., Deutsch, C., Primeau, F., Chang, B., and Devol, A.: Global rates of water-column denitrification derived from nitrogen gas measurements, *Nat. Geosci.*, 5, 547–550, 2012.
- 390 DeVries, T., Deutsch, C., Rafter, P. A., and Primeau, F.: Marine denitrification rates determined from a global 3-D inverse model, *Biogeosciences*, 10, 2481–2496, 2013.
- Dutkiewicz, S., Hickman, A. E., Jahn, O., Gregg, W. W., Mouw, C. B., and Follows, M. J.: Capturing optically important constituents and properties in a marine biogeochemical and ecosystem model, *Biogeosciences*, 12, 4447–4481, 2015.
- 395 Eby, M., Zickfeld, K., Montenegro, A., Archer, D., Meissner, K. J., and Weaver, A. J.: Lifetime of anthropogenic climate change: Time-scales of CO<sub>2</sub> and temperature perturbations, *IOP Conf. Ser.: Earth Environ. Sci.*, 6, 042 015, 2009.
- Eby, M., Weaver, A. J., Alexander, K., Zickfeld, K., Abe-Ouchi, A., Cimadoribus, A. A., Crespin, E., Drijfhout, S. S., Edwards, N. R., Eliseev, A. V., Feulner, G., Fichet, T., Forest, C. E., Goosse, H., Holden, P. B., Joos, F., Kawamiya, M., Kicklighter, D., Kienert, H., Matsumoto, K., Mokhov, I. I., Monier, E., Olsen, S. M., Pedersen, J. O. P., Perrette, M., Philippon-Berthier, G., Ridgwell, A., Schlosser, A., Schneider von Deimling, T., Shaffer, G., Smith, R. S., Spahni, R., Sokolov, A. P., Steinacher, M., Tachiiri, K., Tokos, K., Yoshimori, M., Zeng, N., and Zhao, F.: Historical and idealized climate model experiments: an intercomparison of Earth system models of intermediate complexity, *Clim. Past*, 9, 1111–1140, 2013.
- 400 Engel, A., Kiko, R., and Dengler, M.: Organic Matter Supply and Utilization in Oxygen Minimum Zones, *Ann. Rev. Mar. Sci.*, 14, 355–378, 2022.
- 405 Eppley, R. W.: Temperature and phytoplankton growth in the sea, *Fishery Bulletin*, 70, 1063–1085, 1972.
- Eugster, O. and Gruber, N.: A probabilistic estimate of global marine N-fixation and denitrification, *Global Biogeochem. Cycles*, 26, 2012.
- Fay, A. R. and McKinley, G. A.: Global open-ocean biomes: mean and temporal variability, *Earth System Science Data*, 6, 273–284, 2014.



- Fripiat, F., Martínez-García, A., Marconi, D., Fawcett, S. E., Kopf, S. H., Luu, V. H., Rafter, P. A., Zhang, R., Sigman, D. M., and Haug, G. H.: Nitrogen isotopic constraints on nutrient transport to the upper ocean, *Nat. Geosci.*, 14, 855–861, 2021.
- 410 Garcia, H. E., Locarnini, R. A., Boyer, T. P., Antonov, J. I., Baranova, O. K., Zweng, M. M., Reagan, J. R., and Johnson, D. R.: Dissolved inorganic nutrients (phosphate, nitrate, silicate), *World ocean atlas 2013*, 4, 25–57, 2013a.
- Garcia, H. E., Locarnini, R. A., Boyer, T. P., Antonov, J. I., Mishonov, A. V., Baranova, O. K., Zweng, M. M., Reagan, J. R., and Johnson, D. R.: Dissolved oxygen, apparent oxygen utilization, and oxygen saturation, *World ocean atlas 2013*, 3, 27–61, 2013b.
- Getzlaff, J. and Dietze, H.: Effects of increased isopycnal diffusivity mimicking the unresolved equatorial intermediate current system in an earth system climate model, *Geophysical Research Letters*, 40, 2166–2170, <https://doi.org/10.1002/grl.50419>, 2013.
- 415 Großkopf, T., Mohr, W., Baustian, T., Schunck, H., Gill, D., Kuypers, M. M. M., Lavik, G., Schmitz, R. A., Wallace, D. W. R., and LaRoche, J.: Doubling of marine dinitrogen-fixation rates based on direct measurements, *Nature*, 488, 361–364, 2012.
- Gruber, N. and Sarmiento, J. L.: Global Patterns of marine nitrogen fixation and denitrification, *Global Biogeochemical Cycles*, 11, 235–266, <https://doi.org/10.1029/97GB00077>, 1997.
- 420 Hajima, T., Watanabe, M., Yamamoto, A., Tatebe, H., Noguchi, M. A., Abe, M., Ohgaito, R., Ito, A., Yamazaki, D., Okajima, H., Ito, A., Takata, K., Ogochi, K., Watanabe, S., and Kawamiya, M.: Development of the MIROC-ES2L Earth system model and the evaluation of biogeochemical processes and feedbacks, *Geosci. Model Dev.*, 13, 2197–2244, 2020.
- Hamilton, D. S., Moore, J. K., Arnoeth, A., Bond, T. C., Carslaw, K. S., Hantson, S., Ito, A., Kaplan, J. O., Lindsay, K., Nieradzik, L., Rathod, S. D., Scanza, R. A., and Mahowald, N. M.: Impact of changes to the atmospheric soluble iron deposition flux on ocean biogeochemical cycles in the anthropocene, *Global Biogeochem. Cycles*, 34, e2019GB006448, 2020.
- 425 Holl, C. M. and Montoya, J. P.: Diazotrophic growth of the marine cyanobacterium *Trichodesmium* IMS101 in continuous culture: effects of growth rate on N<sub>2</sub>-fixation rate, biomass, and C:N:P stoichiometry, *J. Phycol.*, 44, 929–937, 2008.
- Houlton, B. Z., Wang, Y.-P., Vitousek, P. M., and Field, C. B.: A unifying framework for dinitrogen fixation in the terrestrial biosphere, *Nature*, 454, 327–330, <https://doi.org/10.1038/nature07028>, 2008.
- 430 Hutchins, D. A. and Capone, D. G.: The marine nitrogen cycle: new developments and global change, *Nat. Rev. Microbiol.*, 2022.
- Johnson, K. S. and Bif, M. B.: Constraint on net primary productivity of the global ocean by Argo oxygen measurements, *Nat. Geosci.*, 14, 769–774, 2021.
- Kalnay, E., Kanamitsu, M., Kistler, R., Collins, W., Deaven, D., Gandin, L., Iredell, M., Saha, S., White, G., Woollen, J., Zhu, Y., Chelliah, M., Ebisuzaki, W., Higgins, W., Janowiak, J., Mo, K. C., Ropelewski, C., Wang, J., Leetmaa, A., Reynolds, R., Jenne, R., and Joseph, D.: The NCEP/NCAR 40-Year Reanalysis Project, *Bull. Am. Meteorol. Soc.*, 77, 437–472, 1996.
- 435 Keller, D. P., Oschlies, A., and Eby, M.: A new marine ecosystem model for the University of Victoria Earth System Climate Model, *Geosci. Model Dev.*, 5, 1195–1220, 2012.
- Kiko, R., Biastoch, A., Brandt, P., Cravatte, S., Hauss, H., Hummels, R., Kriest, I., Marin, F., McDonnell, A. M. P., Oschlies, A., Picheral, M., Schwarzkopf, F. U., Thurnherr, A. M., and Stemmann, L.: Biological and physical influences on marine snowfall at the equator, *Nat. Geosci.*, 10, 852–858, 2017.
- 440 Koeve, W. and Kähler, P.: Heterotrophic denitrification vs. autotrophic anammox – quantifying collateral effects on the oceanic carbon cycle, *Biogeosciences*, 7, 2327–2337, 2010.
- Krishna, S., Pahlow, M., and Schartau, M.: Comparison of two carbon-nitrogen regulatory models calibrated with mesocosm data, *Ecol. Modell.*, 411, 108711, 2019.
- 445 Lam, P. J. and Marchal, O.: Insights into particle cycling from thorium and particle data, *Ann. Rev. Mar. Sci.*, 7, 159–184, 2015.



- Landolfi, A., Oschlies, A., and Sanders, R.: Organic nutrients and excess nitrogen in the North Atlantic subtropical gyre, *Biogeosciences*, 5, 1199–1213, 2008.
- Landolfi, A., Dietze, H., Koeve, W., and Oschlies, A.: Overlooked runaway feedback in the marine nitrogen cycle: the vicious cycle, *Biogeosciences*, 10, 1351–1363, <https://doi.org/10.5194/bg-10-1351-2013>, 2013.
- 450 Landolfi, A., Somes, C. J., Koeve, W., Zamora, L. M., and Oschlies, A.: Oceanic nitrogen cycling and N<sub>2</sub>O flux perturbations in the Anthropocene, *Global Biogeochem. Cycles*, 31, 1236–1255, 2017.
- Longhurst, A. R.: *Ecological Geography of the Sea*, Academic Press, 2007.
- Luo, Y.-W., Doney, S. C., Anderson, L. A., Benavides, M., Berman-Frank, I., Bode, A., Bonnet, S., Boström, K. H., Böttjer, D., Capone, D. G., Carpenter, E. J., Chen, Y. L., Church, M. J., Dore, J. E., Falcón, L. I., Fernández, A., Foster, R. A., Furuya, K., Gómez, F., Gundersen, K., Hynes, A. M., Karl, D. M., Kitajima, S., Langlois, R. J., LaRoche, J., Letelier, R. M., Marañón, E., McGillicuddy, Jr, D. J., Moisaner, P. H., Moore, C. M., Mouriño-Carballido, B., Mulholland, M. R., Needoba, J. A., Orcutt, K. M., Poulton, A. J., Rahav, E., Raimbault, P., Rees, A. P., Riemann, L., Shiozaki, T., Subramaniam, A., Tyrrell, T., Turk-Kubo, K. A., Varela, M., Villareal, T. A., Webb, E. A., White, A. E., Wu, J., and Zehr, J. P.: Database of diazotrophs in global ocean: abundance, biomass and nitrogen fixation rates, *Earth Syst. Sci. Data*, 4, 47–73, 2012.
- 455
- 460 Middelburg, J. J., Soetaert, K., Herman, P. M. J., and Heip, C. H. R.: Denitrification in marine sediments: A model study, *Global Biogeochem. Cycles*, 10, 661–673, 1996.
- Mulholland, M. R. and Bernhardt, P. W.: The effect of growth rate, phosphorus concentration, and temperature on N<sub>2</sub> fixation, carbon fixation, and nitrogen release in continuous cultures of *Trichodesmium* IMS101, *Limnol. Oceanogr.*, 50, 839–849, 2005.
- NASA Goddard Space Flight Center, Ocean Ecology Laboratory, and Ocean Biology Processing Group: MODIS-Aqua Ocean Color Data, [http://dx.doi.org/10.5067/AQUA/MODIS\\_OC.2014.0](http://dx.doi.org/10.5067/AQUA/MODIS_OC.2014.0), accessed: 2018-7-4, 2014.
- 465
- Nickelsen, L., Keller, D. P., and Oschlies, A.: A dynamic marine iron cycle module coupled to the University of Victoria Earth System Model: the Kiel Marine Biogeochemical Model 2 for UVic 2.9, *Geoscientific Model Development*, 8, 1357–1381, <https://doi.org/10.5194/gmd-8-1357-2015>, 2015.
- Pahlow, M. and Prowe, A. E. F.: Model of optimal current feeding in zooplankton, *Mar. Ecol. Prog. Ser.*, 403, 129–144, 2010.
- 470 Pahlow, M., Dietze, H., and Oschlies, A.: Optimality-based model of phytoplankton growth and diazotrophy, *Mar. Ecol. Prog. Ser.*, 489, 1–16, 2013.
- Pahlow, M., Chien, C.-T., Arteaga, L. A., and Oschlies, A.: Optimality-based non-Redfield plankton–ecosystem model (OPEM v1.1) in UVic-ESCM 2.9 – Part 1: Implementation and model behaviour, *Geosci. Model Dev.*, 13, 4663–4690, 2020.
- Paulsen, H., Ilyina, T., Six, K. D., and Stemmler, I.: Incorporating a prognostic representation of marine nitrogen fixers into the global ocean biogeochemical model HAMOCC, *J. Adv. Model. Earth Syst.*, 9, 438–464, 2017.
- 475
- Pavia, F. J., Anderson, R. F., Lam, P. J., Cael, B. B., Vivancos, S. M., Fleisher, M. Q., Lu, Y., Zhang, P., Cheng, H., and Edwards, R. L.: Shallow particulate organic carbon regeneration in the South Pacific Ocean, *Proc. Natl. Acad. Sci. U. S. A.*, 116, 9753–9758, 2019.
- Redfield, A.: On the proportions of organic derivatives in seawater and their relation to the composition of plankton. Daniel, RJ [Ed.] James Johnstone Memorial Volume, 1934.
- 480 Schmidt, H., Getzlaff, J., Löptien, U., and Oschlies, A.: Causes of uncertainties in the representation of the Arabian Sea oxygen minimum zone in CMIP5 models, *Ocean Sci.*, 17, 1303–1320, 2021.
- Shao, Z., Xu, Y., Wang, H., Luo, W., Wang, L., Huang, Y., Agawin, N. S. R., Ahmed, A., Benavides, M., Bentzon-Tilia, M., Berman-Frank, I., Berthelot, H., Biegala, I. C., Bif, M. B., Bode, A., Bonnet, S., Bronk, D. A., Brown, M. V., Campbell, L., Capone, D. G., Carpenter,



- 485 E. J., Cassar, N., Chang, B. X., Chappell, D., Chen, Y.-L. L., Church, M. J., Cornejo-Castillo, F. M., Detoni, A. M. S., Doney, S. C., Dupouy, C., Estrada, M., Fernandez, C., Fernández-Castro, B., Fonseca-Batista, D., Foster, R. A., Furuya, K., Garcia, N., Goto, K., Gago, J., Gradoville, M. R., Hamersley, M. R., Henke, B. A., Hörstmann, C., Jayakumar, A., Jiang, Z., Kao, S.-J., Karl, D. M., Kittu, L. R., Knapp, A. N., Kumar, S., LaRoche, J., Liu, H., Liu, J., Lory, C., Löscher, C. R., Marañón, E., Messer, L. F., Mills, M. M., Mohr, W., Moisaner, P. H., Mahaffey, C., Moore, R., Mouriño-Carballido, B., Mulholland, M. R., Nakaoka, S.-I., Needoba, J. A., Raes, E. J., Rahav, E., Ramírez-Cárdenas, T., Reeder, C. F., Riemann, L., Riou, V., Robidart, J. C., Sarma, V. V. S. S., Sato, T., Saxena, H., Selden, C.,
- 490 Seymour, J. R., Shi, D., Shiozaki, T., Singh, A., Sipler, R. E., Sun, J., Suzuki, K., Takahashi, K., Tan, Y., Tang, W., Tremblay, J.-É., Turk-Kubo, K., Wen, Z., White, A. E., Wilson, S. T., Yoshida, T., Zehr, J. P., Zhang, R., Zhang, Y., and Luo, Y.-W.: Global oceanic diazotroph database version 2 and elevated estimate of global oceanic N<sub>2</sub> fixation, *Earth System Science Data*, 15, 3673–3709, 2023.
- Silsbe, G. M., Behrenfeld, M. J., Halsey, K. H., Milligan, A. J., and Westberry, T. K.: The CAFE model: A net production model for global ocean phytoplankton, *Global Biogeochemical Cycles*, 30, 1756–1777, <https://doi.org/https://doi.org/10.1002/2016GB005521>, 2016.
- 495 Somes, C. J. and Oschlies, A.: On the influence of “non-Redfield” dissolved organic nutrient dynamics on the spatial distribution of N<sub>2</sub> fixation and the size of the marine fixed nitrogen inventory, *Global Biogeochem. Cycles*, 29, 973–993, 2015.
- Somes, C. J., Schmittner, A., and Altabet, M. A.: Nitrogen isotope simulations show the importance of atmospheric iron deposition for nitrogen fixation across the Pacific Ocean, *Geophysical Research Letters*, 37, <https://doi.org/https://doi.org/10.1029/2010GL044537>, 2010a.
- Somes, C. J., Schmittner, A., Galbraith, E. D., Lehmann, M. F., Altabet, M. A., Montoya, J. P., Letelier, R. M., Mix, A. C., Bourbonnais, A., and Eby, M.: Simulating the global distribution of nitrogen isotopes in the ocean, *Global Biogeochemical Cycles*, 24, <https://doi.org/https://doi.org/10.1029/2009GB003767>, 2010b.
- 500 Somes, C. J., Oschlies, A., and Schmittner, A.: Isotopic constraints on the pre-industrial oceanic nitrogen budget, *Biogeosciences*, 10, 5889–5910, 2013.
- Wang, W.-L., Moore, J. K., Martiny, A. C., and Primeau, F. W.: Convergent estimates of marine nitrogen fixation, *Nature*, 566, 205–211, 2019.
- 505 Weaver, A. J., Eby, M., Wiebe, E. C., Bitz, C. M., Duffy, P. B., Ewen, T. L., Fanning, A. F., Holland, M. M., MacFadyen, A., Matthews, H. D., Meissner, K. J., Saenko, O., Schmittner, A., Wang, H., and Yoshimori, M.: The UVic earth system climate model: Model description, climatology, and applications to past, present and future climates, *Atmosphere-Ocean*, 39, 361–428, 2001.
- Weber, T. and Deutsch, C.: Local versus basin-scale limitation of marine nitrogen fixation, *Proc. Natl. Acad. Sci. U. S. A.*, 111, 8741–8746, 2014.
- 510 Wrightson, L. and Tagliabue, A.: Quantifying the Impact of Climate Change on Marine Diazotrophy: Insights From Earth System Models, *Frontiers in Marine Science*, 7, 2020.